

Complete oxidation of acetaldehyde over a composite photocatalyst of graphitic carbon nitride and tungsten(VI) oxide under visible-light irradiation

Zhengyuan Jin^a, Naoya Murakami^a, Toshiki Tsubota^a, Teruhisa Ohno^{a, b, c, *}

^a Department of Applied Chemistry, Faculty of Engineering, Kyushu Institute of Technology, 1-1 Sensuicho, Tobata, Kitakyushu 804-8550, Japan

^b JST, PRESTO, 4-1-8 Honcho Kawaguchi, Saitama 332-0012, Japan

^c JST, ACT-C, 4-1-8 Honcho Kawaguchi, Saitama 332-0012, Japan

*Corresponding author

Tel and fax: 81-93-884-3318

E-mail: tohno@che.kyutech.ac.jp

Abstract

Graphitic carbon nitride (g-C₃N₄) was prepared by heating melamine and then its specific surface area was enlarged by hydrothermal treatment in aqueous sodium hydroxide solution. The g-C₃N₄ samples **were blended with** tungsten(VI) oxide (WO₃) using a planetary mill in order to improve photocatalytic activity. The composite photocatalyst with optimized amounts of these contents showed higher photocatalytic activity for decomposition of acetaldehyde under visible-light irradiation than did original samples. From the results, we concluded that the composite photocatalyst utilizes both high oxidation ability of WO₃ and high reduction ability of g-C₃N₄ by Z-scheme charge transfer.

Keyword: g-C₃N₄; WO₃; photocatalysis; planetary mill; Z-scheme.

1. Introduction

Titanium(IV) oxide (TiO_2) is the most widely used photocatalyst because of its excellent oxidation ability, availability and stability [1]. However, there are two major problems with a conventional TiO_2 photocatalyst: it is inactive under visible-light irradiation and it has low quantum efficiency due to a high recombination rate of photogenerated electron-hole pairs. There have been numerous studies on TiO_2 with impurity doping [2, 3], co-catalyst loading [4] and shape control [5, 6] for improvement of visible-light response and reaction efficiency of electrons and holes, though these methods still have limitations for improvement of solar energy conversion efficiency.

It is rather challenging to design a semiconductor photocatalyst fulfilling the multiple requirements. Actually, a single semiconductor with large visible-light absorption has difficulty in exhibiting both high reduction and oxidation abilities due to its narrow bandgap structure. Therefore, a composite photocatalyst consisting of different kinds of semiconductors has been studied in recent years. Some studies showed that an appropriate composition of two kinds of photocatalyst enhanced photocatalytic activity as a result of charge separation between two semiconductors [7-12]. This mechanism employs interparticle electron transfer to one semiconductor with a more positive conduction band (CB) potential and hole transfer to the other semiconductor with a more negative valence band (VB) potential. Thus, this kind of composite photocatalyst cannot utilize both high reduction and oxidation abilities. In contrast, another reaction mechanism for a composite photocatalyst, namely, Z-scheme reaction mechanism, has been suggested in several reports [13-17]. This mechanism enables a composite photocatalyst to utilize both reduction ability for one semiconductor with more negative CB potential and oxidation ability for another semiconductor with more positive VB potential as a result of two-step excitation. Thus, a Z-scheme composite photocatalyst is one means for utilizing both high oxidation and reduction abilities under visible-light irradiation if appropriate semiconductors are used.

In our previous study, a composite of graphitic carbon nitride ($\text{g-C}_3\text{N}_4$), which is an organic semiconductor with visible-light absorption, high reduction ability and high chemical stability [18], with sulfur-doped TiO_2 was made [19]. In that study, the composite sample prepared by a planetary mill showed high photocatalytic activity for acetaldehyde decomposition under visible-light irradiation as a result of

Z-scheme charge transfer. Thus, the sample showed both high oxidation ability of sulfur-doped TiO_2 and high reduction ability of $\text{g-C}_3\text{N}_4$. However, it was concluded that photoabsorption of sulfur-doped TiO_2 and small specific surface area of $\text{g-C}_3\text{N}_4$ are bottlenecks for further enhancement of photocatalytic activity.

Tungsten(VI) oxide (WO_3) may be ideal for a combination pair with $\text{g-C}_3\text{N}_4$ in the Z-scheme reaction because it is well known as an oxidation part photocatalyst for Z-scheme photocatalytic water splitting [14]. Moreover, it has larger visible-light absorption than that of sulfur-doped TiO_2 . WO_3 without a co-catalyst is thought to be inappropriate for organic decomposition due to inferior reductive potential of the CB for one-electron reduction of oxygen (O_2). Therefore, a co-catalyst metal for multi-electron reduction of O_2 [20, 21] or a reduction part semiconductor with sufficient negative CB potential for one-electron reduction of O_2 in the Z-scheme reaction [15-17] is necessary for complete oxidation of organic compounds over WO_3 . Although there have been some reports of composite photocatalysts with $\text{g-C}_3\text{N}_4$ including $\text{g-C}_3\text{N}_4/\text{WO}_3$ [7, 9-11, 22-24], a charge separation mechanism was employed in those photocatalysts, and explanation of the mechanism was not sufficient. Complete oxidation of organic compounds into carbon dioxide (CO_2) was not discussed in photocatalytic evaluation.

In this study, a composite of $\text{g-C}_3\text{N}_4$, which was prepared by heat treatment of melamine [25], and WO_3 was prepared by using a planetary mill and its photocatalytic activity for acetaldehyde decomposition was discussed from the viewpoint of complete oxidation into CO_2 . Moreover, $\text{g-C}_3\text{N}_4$ with a large specific surface area, which was obtained by hydrothermal treatment of original $\text{g-C}_3\text{N}_4$ in sodium hydroxide (NaOH) solution [26], was used for the composite photocatalyst in order to improve photocatalytic activity.

2. Experimental

2.1. Materials

All chemicals were reagent grade and used without further purification. $\text{g-C}_3\text{N}_4$ powder was synthesized by heating 30 g of melamine at 823 K at a heating rate of $9\text{ K}\cdot\text{min}^{-1}$, followed by heating for 4 hours at that temperature. The product was collected and ground into powder. WO_3 powders were commercial samples (Kojundo Chemical Laboratory Co.).

2.2. Hydrothermal treatment of $\text{g-C}_3\text{N}_4$ in NaOH solution

The specific surface area of g-C₃N₄ was enlarged by hydrothermal method [26]. One gram of as-prepared g-C₃N₄ powder was added to 50 mL of 0.1 M aqueous NaOH solution. The suspension was ultrasonicated for 10 min to completely disperse the g-C₃N₄, and then it was heated in a Teflon-lined autoclave at 373 K for 24 hours. After the treatment, the precipitates were centrifuged and washed with deionized water several times to remove Na⁺ ion and then dried in a vacuum drying oven at 333 K overnight. This sample is denoted as HT-g-C₃N₄.

2.3 Preparation of a composite photocatalyst by a planetary mill

The composite sample of WO₃ and original g-C₃N₄ was prepared as follows. One gram of WO₃ and original g-C₃N₄ powder and 20 mL of deionized water were added to a 50 mL agate bowl containing 50 g of yttrium-stabilized zirconia grinding beads (Nikkato Co., ϕ = 0.6 mm). Then the agate bowl was put on a planetary mill (Fritsch Japan Co., Planetary Micro Mill pulverisette 7) and the planetary mill was operated at 750 rpm for 10 min. After removing the beads by screening, the sample was separated by filtration, washed with deionized water several times, and dried in a vacuum drying oven at 333 K overnight. This composite sample is denoted as CNW_x, where x is the weight percent of WO₃ included in the composite sample. The composite sample of WO₃ and HT-g-C₃N₄ was prepared by the same procedure as that for CNW_x. This composite sample is denoted as HTW_x. As a reference, each sample, i.e., original g-C₃N₄, HT-g-C₃N₄ and WO₃, was treated by the same procedure. These composite samples are denoted as CNW₀, HTW₀ and PM-WO₃, respectively.

2.4. Characterization

Crystal structures of the obtained samples were characterized by an X-ray diffractometer (Rigaku, MiniFlex II) equipped with a Cu K α irradiation source. The morphology of prepared particles was observed by field emission scanning electron microscopy (FE-SEM; JEOL, JSM-6701FONO). Diffuse reflectance spectra (DRS) were measured using a UV-vis spectrophotometer (Shimadzu, UV-2600) equipped with an integrating sphere unit (Shimadzu, ISR-2600 Plus). Specific surface area (S_{BET}) was determined with a surface area analyzer (Quantachrome, Nova 4200e) by the Brunauer-Emmett-Teller method. Functional group vibrations were confirmed by using a Fourier transform infrared spectrometer (FTIR; JASCO, FT / IR

4200) with a diffuse reflectance accessory (JASCO, DR-81). Fluorescence spectra were obtained using a photoluminescence spectrometer (JASCO, FP-8500).

2.5. Photocatalytic measurement

Before evaluation of the photocatalytic activity, each sample was irradiated with UV light using black light (UVP, XX-15BLB) in order to remove organic contaminants on the sample. The photocatalytic activity of the composite sample was evaluated by CO₂ liberation from photocatalytic mineralization of acetaldehyde. One hundred milligrams of powder, which has complete extinction of incident radiation, was spread on the bottom of a glass dish, and the glass dish was placed in a Tedlar bag (AS ONE Co. Ltd.). Then 125 cm³ artificial air containing 1000 ppm of acetaldehyde was injected into the bag. Photoirradiation was performed at room temperature after the acetaldehyde had reached adsorption equilibrium. A light-emitting diode (LED; Epitex, L435-30M32L), which emitted light at wavelengths of ca. 435 nm, was used as a light source, and its intensity was controlled by 1.0 mW cm⁻². The concentration of CO₂ was observed by gas chromatography (Shimadzu GC-8A, FID detector) equipped with a Porapak N packed column and a methanizer (GL Science, MT-221) as a function of irradiation time.

3. Results and discussion

3.1. Characterization of g-C₃N₄ and HT-g-C₃N₄

Figure 1A shows X-ray diffraction (XRD) patterns of original g-C₃N₄ and HT-g-C₃N₄ samples. The original g-C₃N₄ had two peaks at 13.1° and 27.6°, which can be indexed as (100) and (002) diffraction planes (JCPDS 87-1526). Similarly, the XRD pattern of HT-g-C₃N₄ also had characteristic peaks at 27.6°, suggesting that HT-g-C₃N₄ has the same crystal structure as that of original g-C₃N₄ (Fig. 1C). The low-angle reflection peak at 13.1° becomes less pronounced due to decreased planar size of the layers during NaOH solution etching of original g-C₃N₄ [26, 27]. Functional groups of original g-C₃N₄ and HT-g-C₃N₄ were confirmed by FT-IR spectroscopy. As shown in Fig. 1B, the characteristic IR spectrum of HT-g-C₃N₄ was similar to that of original g-C₃N₄: a peak at about 810 cm⁻¹ originating from the heptazine ring system and peaks in the region from 900 to 1800 cm⁻¹ attributed to either trigonal C-N(-C)-C or bridging C-NH-C units

were observed in both samples. UV-vis **DRS** are shown in Fig. 1C. Compared with the spectrum of original g-C₃N₄, the spectrum of HT-g-C₃N₄ was shifted to longer wavelengths. A similar blue shift of peak wavelength was observed in fluorescence emission spectra (Fig. 1D). These results are presumably due to decrease in particle size [27, 28]. Actually, the S_{BET} of g-C₃N₄ was enlarged from 11 m² g⁻¹ to 50 m² g⁻¹ by hydrothermal treatment. Fig. 2 shows SEM images of original g-C₃N₄ and HT-g-C₃N₄ samples. The original g-C₃N₄ was plate-like particles (Fig. 2A), while HT-g-C₃N₄ had an uneven surface (Fig. 2B). This indicates that the surface of g-C₃N₄ particles was etched by hydrothermal treatment in NaOH solution, resulting in enlargement of S_{BET} without any change in crystal structure. These results coincide with the results of **reported study** [26].

Photocatalytic activity of original g-C₃N₄ and HT-g-C₃N₄ was evaluated by CO₂ liberation from decomposition of acetaldehyde. Figure 3 shows the time courses of CO₂ liberation over original g-C₃N₄ and HT-g-C₃N₄. Although HT-g-C₃N₄ showed smaller visible-light absorption than that of original g-C₃N₄, it showed 3-times greater CO₂ liberation due to large S_{BET} , which increase in adsorption, reduction and oxidation sites. However, CO₂ liberation for 48 hours was much smaller than 2000 ppm, which means complete decomposition of acetaldehyde into CO₂, due its low oxidation ability [19].

3.2. Characterization of CNW_x and HTW_x

Powder XRD patterns of CNW_x samples are shown in Fig. 4A. XRD patterns showed only peaks attributed to g-C₃N₄ and WO₃, and peaks attributed to other components were not detected. Although a peak at 27.6°, which was attributed to (002) of g-C₃N₄, was observed in XRD patterns of CNW_x ($x < 50$) samples, XRD patterns of CNW_x ($x > 50$) samples showed no appreciable peak around 27.6° due to weak diffraction intensity of g-C₃N₄. On the other hand, peaks attributed to WO₃ could be observed in all CNW_x samples ($x > 0$), and no changes in peak pattern and width of the peak at 24.3° were observed, compared with original WO₃ (Fig. 4, S1). This is reasonable since PM-WO₃ showed the same pattern and width of peak at 24.3° as original WO₃. In contrast, CNW₀ showed a larger peak width at 27.6° than that of original g-C₃N₄. This result coincides with enlargement of S_{BET} by planetary mill treatment (Fig. 5). A similar result was obtained for HTW_x samples (Fig. 4B).

Figure 6 shows SEM images of PM-WO₃, CNW_x and HTW_x. PM-WO₃ showed aggregated particles with

particle size of a few hundreds of nanometers (Fig. 5), and the morphology and S_{BET} of WO_3 particles were slightly changed by planetary mill treatment (Fig. 5). On the other hand, plate-like particles were pulverized into small particles by the planetary mill treatment in SEM images of CNW0 and HTW0 samples (Fig. S2). This agreed with increase in S_{BET} (Fig. 5). For CNW x ($x > 0$) samples, it seemed that WO_3 particles attached to the surface of g- C_3N_4 increased with an increase in WO_3 content. When the WO_3 content was above 80 wt%, the g- C_3N_4 particles were almost completely covered by WO_3 particles. The same result was also found in HTW x ($x > 0$) samples.

Figure 7 shows UV-vis **DRS** of PM- WO_3 , CNW x and HTW x . **DRS** of CNW0 and HTW0 were blue-shifted compared with those of original g- C_3N_4 and HT-g- C_3N_4 (Fig. S3). This blue shift is presumably due to decrease in particle size by planetary mill treatment [27, 28], as observed in S_{BET} . Photoabsorption at the wavelength of 435 nm of HTW x samples increased with increase in WO_3 content, and it was smaller than CNW x (Fig. 8A). This is because PM- WO_3 has the largest photoabsorption at the wavelength of 435 nm, followed in order by CNW0 and HTW0. On the other hand, photoabsorption at a longer wavelength of 500 nm, which was observed in the **DRS** of WO_3 , was suppressed by composition with a small amount of g- C_3N_4 . Figure 8B shows relative reflectance of CNW x and HTW x samples at the wavelength of 800 nm as a function of WO_3 content. CNW x and HTW x samples showed no linear relationship between relative reflectance at the wavelength of 800 nm and WO_3 content. Since photoabsorption at a longer wavelength of 500 nm is attributed to the W^{5+} state in WO_3 , which is generated by electron accumulation in WO_3 and reduction treatment of WO_3 [29-31], a nonlinear relationship means that electron accumulation in WO_3 was decreased by composition with g- C_3N_4 . A similar phenomenon was observed in the Z-scheme composite photocatalyst of WO_3 and CaFe_2O_4 [13].

3.3. Photocatalytic activity for acetaldehyde decomposition

The photocatalytic activities of the prepared samples were evaluated by CO_2 liberation from photocatalytic mineralization of acetaldehyde. Figure 9A shows the time courses of CO_2 liberation of the CNW x samples and PM- WO_3 . WO_3 showed a high CO_2 liberation rate at the beginning of photoirradiation, but CO_2 liberation stopped with longer photoirradiation before reaching 2000 ppm, which means complete decomposition of 1000 ppm acetaldehyde. WO_3 can partially decompose acetaldehyde to formaldehyde or

formic acid with CO₂ liberation [15], but it cannot completely decompose these molecules to CO₂ without efficient electron consumption [16]. In contrast, almost all of the composite samples showed no saturation tendency of CO₂ liberation with irradiation time and a larger amount of CO₂ liberation for 48 hours. This implies that electron consumption in WO₃ was promoted by composition with g-C₃N₄, as observed in WO₃ composed with other semiconductors or metals [15-17, 20, 21]. Actually, results from UV-vis **DRS** of CNW_x and HTW_x samples indicate that electron accumulation in WO₃ is suppressed by composition of g-C₃N₄ (Fig. 8B). Since g-C₃N₄ is a semiconductor with more negative CB potential than that of WO₃ and one-electron reduction potential of O₂, a plausible mechanism is Z-scheme reaction accompanied by electron transfer from the CB of WO₃ to the VB of g-C₃N₄ (Fig. 10). Thus, all WO₃ particles are required to be attached on all g-C₃N₄ particles for efficient charge transfer. Otherwise, acetaldehyde on non-composite g-C₃N₄ and WO₃ remained without being decomposed completely into CO₂. This is the reason why CNW_x with a large amount of WO₃ showed a saturation tendency and CNW_x with a small amount of WO₃ showed a low rate of CO₂ liberation.

Figure 9B shows the time courses of CO₂ liberation of the HTW_x composites and PM-WO₃. HTW_x samples also showed similar enhancement for CO₂ liberation by the composition as observed in CNW_x samples. However, HTW_x ($x > 0$) samples showed slightly larger CO₂ liberation than that of CNW_x ($x > 0$), though CO₂ liberation of HTW₀ was twice larger than that of CNW₀ for 48 hours. This can be explained as follows. g-C₃N₄ in composite samples predominantly works as not an adsorption and oxidation site for organic compounds but a reduction site for O₂, while adsorption, oxidation and reduction must all proceed on single g-C₃N₄. Therefore, enhancement of S_{BET} of g-C₃N₄ in a composite sample is thought to show no direct contribution to oxidation of acetaldehyde because acetaldehyde is hardly decomposed over g-C₃N₄ in the composite photocatalyst.

Figure 9C shows CO₂ liberation for 48 hours of CNW_x and HTW_x samples as a function of WO₃ content. A volcano-like relationship was observed in both CNW_x and HTW_x samples, but HTW_x samples with a larger amount of WO₃ showed larger CO₂ liberation because larger S_{BET} of g-C₃N₄ in HTW_x samples increased contact points between g-C₃N₄ and WO₃. However, optimized HTW_x showed slightly larger CO₂ liberation than that of CNW_x, and the optimum ratio of WO₃ in HTW_x samples was the same as that in CNW_x samples despite larger S_{BET}. This is due to smaller photoabsorption of HTW₀ than that of CNW₀, as

seen in Fig. 8A.

Figure 9D shows UV-vis DRS of PM-WO₃, CNW50 and HTW50 before and after photocatalytic reaction. After photocatalytic reaction, photoabsorption of PM-WO₃ at wavelengths from 500 nm to 800 nm showed greatly increased, which is attributed to the partial reduction of W⁶⁺ to W⁵⁺ by photoexcited electrons. In the case of CNW50 and HTW50, no obvious changes can be found from DRS of the composite photocatalysts before and after photocatalytic reaction. The results indicate that the self-reduction process by photogenerated electrons in WO₃ are prevented after composite with g-C₃N₄ or HT-g-C₃N₄, because photogenerated electrons in CB of WO₃ should be efficiently consumed by the reaction with photogenerated holes in VB of g-C₃N₄ or HT-g-C₃N₄. This means that the composite photocatalysts follow Z-scheme charge separation mechanism.

Larger CO₂ liberation over composite samples may be attributed to decomposition of g-C₃N₄. Therefore, we confirmed stability of g-C₃N₄ in the prepared samples by a self-decomposition test. Figure S4 shows the time courses of CO₂ liberation over CNW50 and HTW50 in the presence and absence of acetaldehyde. Although slight CO₂ liberation was observed in CNW50 and HTW50 samples, it was much smaller than CO₂ liberation in the presence of acetaldehyde. This confirmed that enlargement of CO₂ was not due to decomposition of g-C₃N₄. In the HTW50 sample, 1600 ppm of CO₂ was observed after 48 hours of photoirradiation, indicating that at least 600 ppm of acetaldehyde had been completely decomposed into 1200 ppm of CO₂. This “partial complete oxidation” is also collateral evidence for Z-scheme charge transfer in the composite photocatalyst because complete oxidation of acetaldehyde into CO₂ cannot occur over WO₃ without a metal co-catalyst or semiconductor for Z-scheme charge transfer.

4. Conclusions

In this study, a highly active photocatalyst under visible-light irradiation for organic decomposition was synthesized by a composite of g-C₃N₄ and WO₃ using a planetary mill. UV-vis **DRS** and photocatalytic evaluation indicated that the composite photocatalysts show high activity as a result of Z-scheme reaction. The optimized composite samples prepared in the present study showed complete oxidation of “most of all” acetaldehyde into CO₂ by Z-scheme reaction, unlike previously reported composite photocatalysts [22-24]. For further enhancement of photocatalytic activity under visible-light irradiation, a composite photocatalyst

with both large visible-light absorption and a large number of contact points between g-C₃N₄ and WO₃ is needed.

Acknowledgments

This work was supported by the JST PRESTO program and the JST ACT-C program.

References

- [1] K. Hashimoto, H. Irie, A. Fujishima, *Japanese Journal of Applied Physics* 44 (2005) 8269-8285.
- [2] T. Ohno, M. Akiyoshi, T. Umebayashi, K. Asai, T. Mitsui, M. Matsumura, *Applied Catalysis A: General* 265 (2004) 115-121.
- [3] T. Ohno, T. Tsubota, K. Nishijima, Z. Miyamoto, *Chemistry Letters* 33 (2004) 750–751.
- [4] S. Sato, J. M. White, *Journal of the American Chemical Society* 102 (1980) 7206-7210.
- [5] N. Murakami, Y. Kurihara, T. Tsubota, T. Ohno, *The Journal of Physical Chemistry C* 113 (2009) 3062-3069.
- [6] T. Ohno, K. Sarukawa, M. Matsumura, *New Journal of Chemistry* 26 (2002) 1167-1170.
- [7] S.C. Yan, S.B. Lv, Z.S. Li, Z.G. Zou, *Dalton Transactions* 39 (2010) 1488-1491.
- [8] A.K. Chakraborty, M.A. Kebede, *Reaction Kinetics, Mechanisms and Catalysis* 106 (2012) 83-98.
- [9] Q. Xiang, J. Yu, M. Jaroniec, *The Journal of Physical Chemistry C* 115 (2011) 7355–7363.
- [10] G.Z. Liao, S. Chen, X. Quan, H.T. Yu, H.M. Zhao, *Journal of Materials Chemistry* 22 (2012) 2721-2726.
- [11] C. Pan, J. Xu, Y. Wang, D. Li, Y. Zhu, *Advanced Functional Materials* 22 (2012) 1518–1524.
- [12] N. Serpone, P. Maruthamuthu, P. Pichat, E. Pelizzetti, H. Hidaka, *Journal of Photochemistry and Photobiology A: Chemistry* 85 (1995) 247–255.
- [13] Z.F. Liu, Z.G. Zhao, M. Miyauchi, *Journal of Physical Chemistry C* 113 (2009) 17132-17137.
- [14] R. Abe, *Bulletin of the Chemical Society of Japan* 84 (2011) 1000-1030.
- [15] T. Arai, M. Horiguchi, M. Yanagida, T. Gunji, H. Sugihara, K. Sayama, *Journal of Physical Chemistry C* 113 (2009) 6602–6609.
- [16] T. Arai, M. Yanagida, Y. Konishi, Y. Iwasaki, H. Sugihara, K. Sayama, *Catalysis Communications* 9 (2008) 1254–1258.
- [17] T. Arai, M. Yanagida, Y. Konishi, Y. Iwasaki, H. Sugihara, K. Sayama, *Journal of Physical Chemistry C* 111 (2007) 7574-7577.
- [18] X.C. Wang, K. Maeda, A. Thomas, K. Takanabe, G. Xin, J.M. Carlsson, K. Domen, M. Antonietti, *Nature Materials* 8 (2009) 76-80.
- [19] K. Kondo, N. Murakami, C. Ye, T. Tsubota, T. Ohno, *Applied Catalysis B: Environmental* 142–143 (2013) 362– 367.
- [20] R. Abe, H. Takami, N. Murakami, B. Ohtani, *Journal of the American Chemical Society* 130 (2008) 7780–7781.
- [21] T. Arai, M. Horiguchi, M. Yanagida, T. Gunji, H. Sugihara, K. Sayama, *Chemical Communications* (2008) 5565–5567.
- [22] K. Katsumata, R. Motoyoshi, N. Matsushita, K. Okada, *Journal of Hazardous Materials* 260 (2013) 475–482.
- [23] H. Yan, X. Zhang, S. Zhou, X. Xie, Y. Luo, Y. Yu, *Journal of Alloys and Compounds* 509 (2011) L232–L235.
- [24] L. Huang, H. Xu, Y. Li, H. Li, X. Cheng, J. Xia, Y. Xua, *Guobin Caia, Dalton Transactions* 42 (2013) 8606-8616.
- [25] S.C. Yan, Z.S. Li, Z.G. Zou, *Langmuir* 25 (2009) 10397–10401.
- [26] T. Sano, S. Tsutsui, K. Koike, T. Hirakawa, Y. Teramoto, N. Negishi, K. Takeuchi, *Journal of Materials*

Chemistry A 1 (2013) 6489-6496.

[27] M. Groenewolt, M. Antonietti, *Advanced Materials* 17 (2005) 1789–1792.

[28] P. Niu, L.L. Zhang, G. Liu, H.M. Cheng, *Advanced Functional Materials* 22 (2012) 4763-4770.

[29] M. Fujii, T. Kawai, H. Nakamatsu, S. Kawai, *Journal of the Chemical Society-Chemical Communications* (1983) 1428-1429.

[30] Y. He, Z. Wu, L. Fu, C. Li, Y. Miao, L. Cao, H. Fan, B. Zou, *Chemistry of Materials* 15 (2003) 4039-4045.

[31] M. Miyauchi, M. Shibuya, Z. Zhao, Z. Liu, *Journal of Physical Chemistry C* 113 (2009) 10642–10646.

[32] J.S. Zhang, X.F. Chen, K. Takanabe, K. Maeda, K. Domen, J.D. Epping, X.Z. Fu, M. Antonietti, X.C. Wang, *Angewandte Chemie-International Edition* 49 (2010) 441–444.

[33] Y. Xu, M.A.A. Schoonen, *American Mineralogist* 85 (2000) 543-556.

Figure Captions

Fig. 1 (A) XRD patterns, (B) FTIR spectra, (C) UV-vis **DRS** and (D) fluorescence emission spectra under excitation at the wavelength of 365 nm of original g-C₃N₄ and HT-g-C₃N₄.

Fig. 2 SEM images of (A) original g-C₃N₄ and (B) HT-g-C₃N₄.

Fig. 3 Time courses of CO₂ liberation from acetaldehyde decomposition over original g-C₃N₄ and HT-g-C₃N₄.

Fig. 4 XRD patterns of original WO₃, PM-WO₃, CNW_x and HTW_x samples.

Fig. 5 S_{BET} of original g-C₃N₄, HT-g-C₃N₄, original WO₃, PM-WO₃, CNW_x and HTW_x samples as a function of WO₃ content.

Fig. 6 SEM images of original WO₃, PM-WO₃, CNW_x and HTW_x samples with 250 nm size bar.

Fig. 7 UV-vis **DRS** of (A) CNW_x, (B) HTW_x and PM-WO₃ samples.

Fig. 8 Relative reflectance of CNW_x and HTW_x samples at the wavelengths of (A) 435 nm and (B) 800 nm as a function of WO₃ content.

Fig. 9 Time courses of CO₂ liberation from acetaldehyde decomposition over (A) CNW_x and (B) HTW_x samples. (C) CO₂ liberation over CNW_x and HTW_x samples for 48 hours of photoirradiation as a function of WO₃ content. (D) UV-vis **DRS** of PM-WO₃, CNW₅₀ and HTW₅₀ before and after photocatalytic reaction.

Fig. 10 Schematic band structure of g-C₃N₄ and WO₃. The literature values for the band structure of g-C₃N₄ [32] and WO₃ [33] were used.

Figure

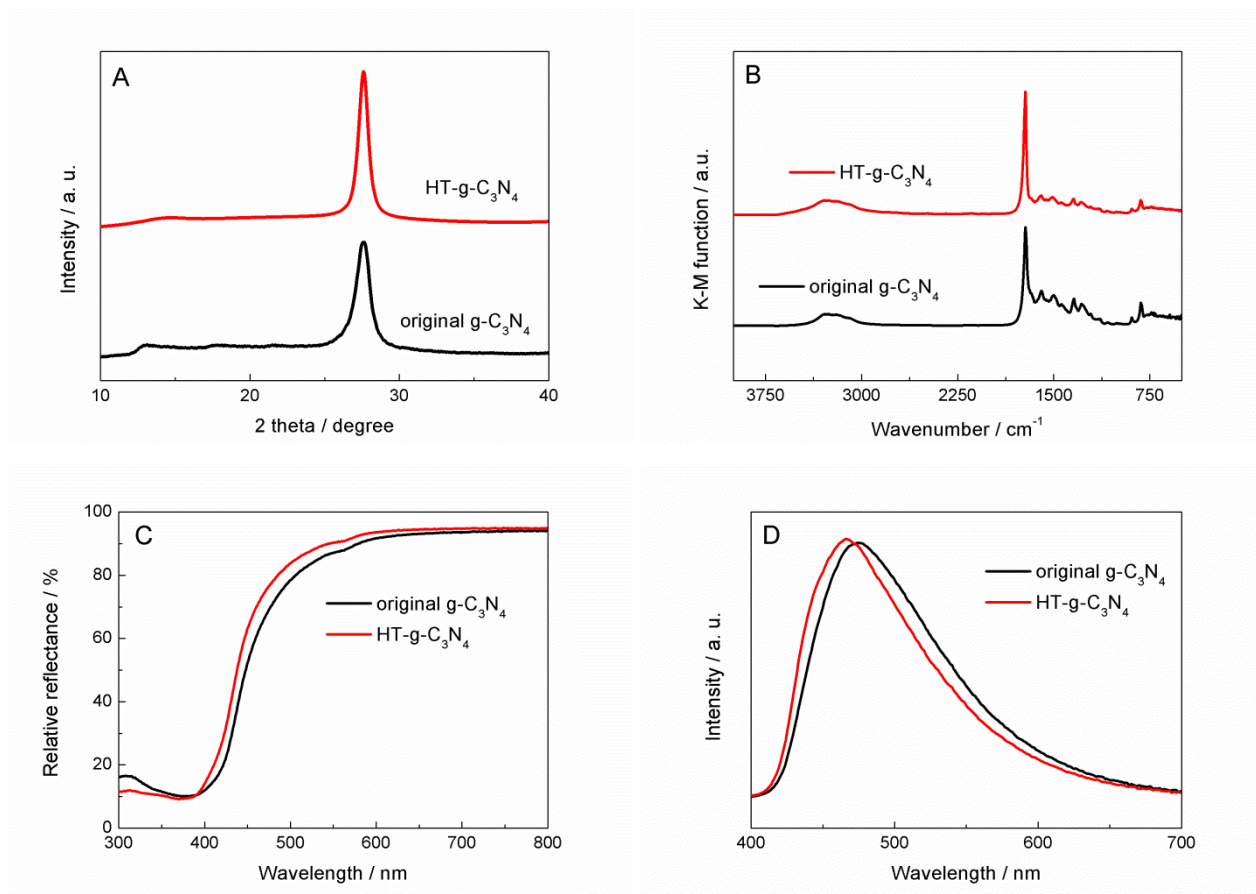


Fig. 1 (A) XRD patterns, (B) FTIR spectra, (C) UV-vis DR spectra and (D) fluorescence emission spectra under excitation at the wavelength of 365 nm of original $\text{g-C}_3\text{N}_4$ and HT- $\text{g-C}_3\text{N}_4$.

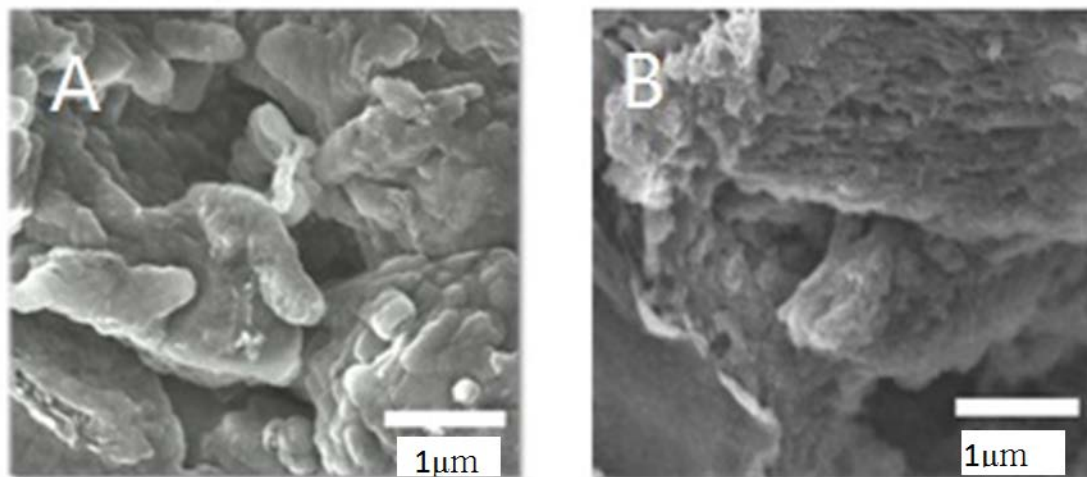


Fig. 2 SEM images of (A) original $\text{g-C}_3\text{N}_4$ and (B) HT- $\text{g-C}_3\text{N}_4$.

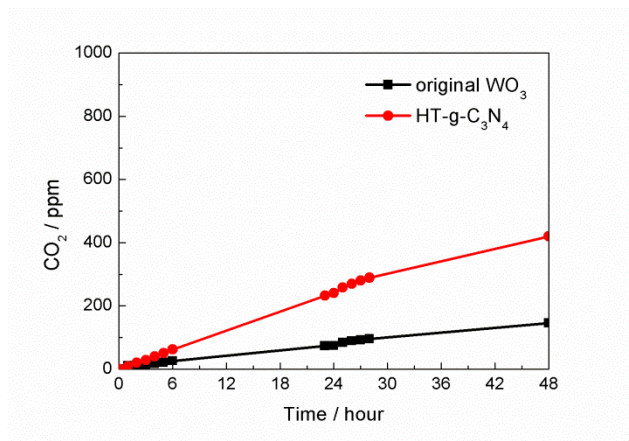


Fig. 3 Time courses of CO_2 liberation from acetaldehyde decomposition over original $\text{g-C}_3\text{N}_4$ and HT- $\text{g-C}_3\text{N}_4$.

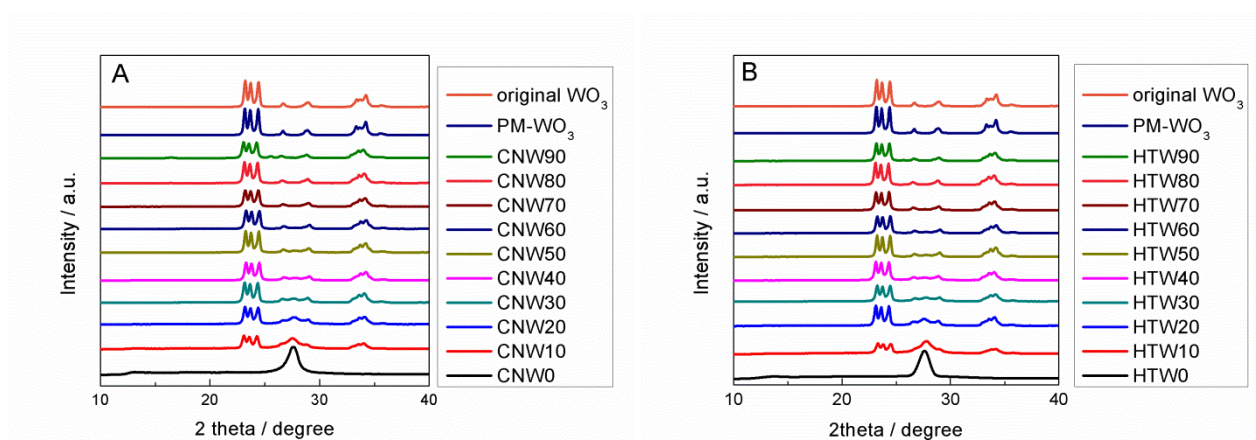


Fig. 4 XRD patterns of original WO_3 , PM- WO_3 , CNW x and HTW x samples.

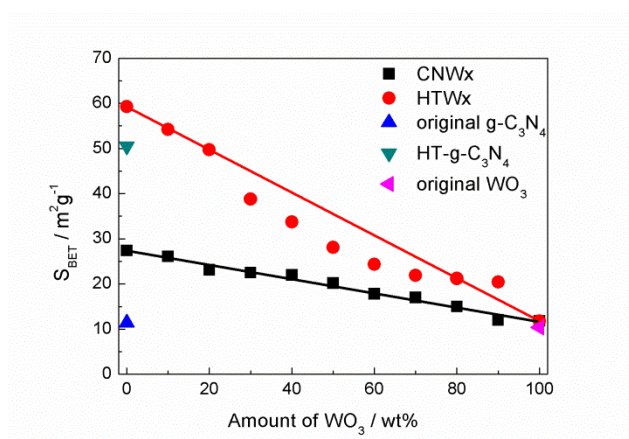


Fig. 5 S_{BET} of original $\text{g-C}_3\text{N}_4$, HT- $\text{g-C}_3\text{N}_4$, original WO_3 , PM- WO_3 , CNW x and HTW x samples as a function of WO_3 contents.

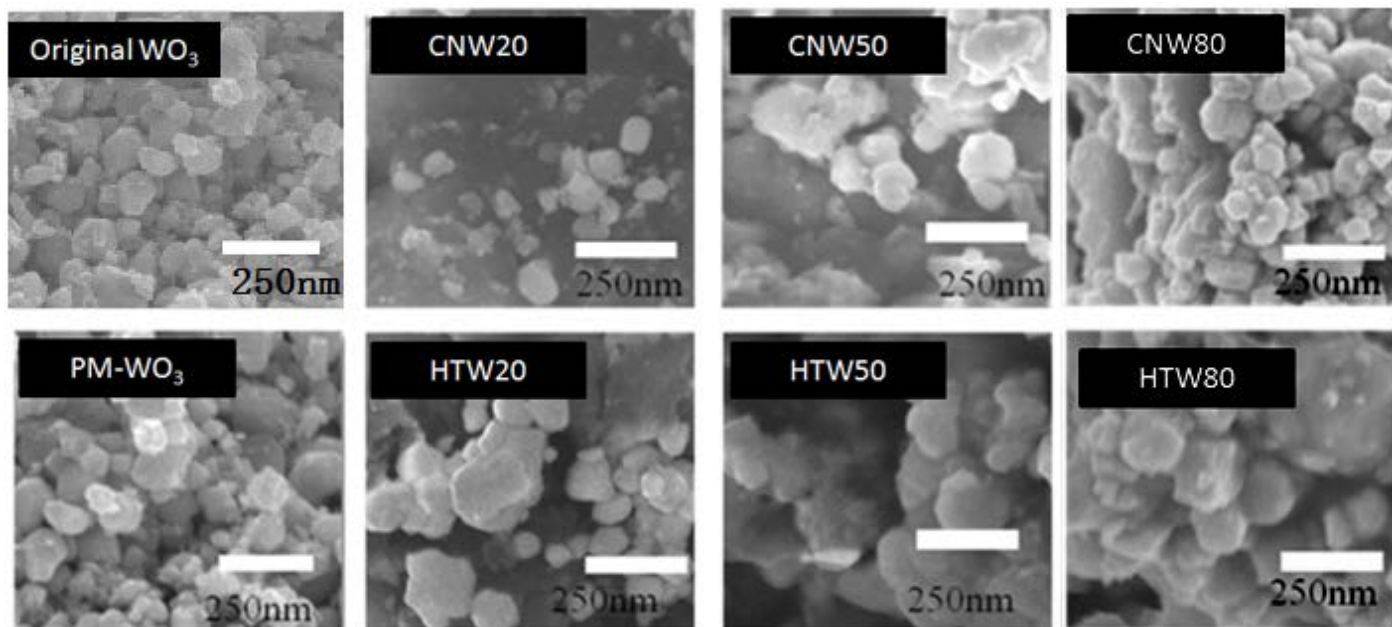


Fig. 6 SEM images of original WO_3 , PM- WO_3 , CNW x and HTW x samples with 250 nm size bar.

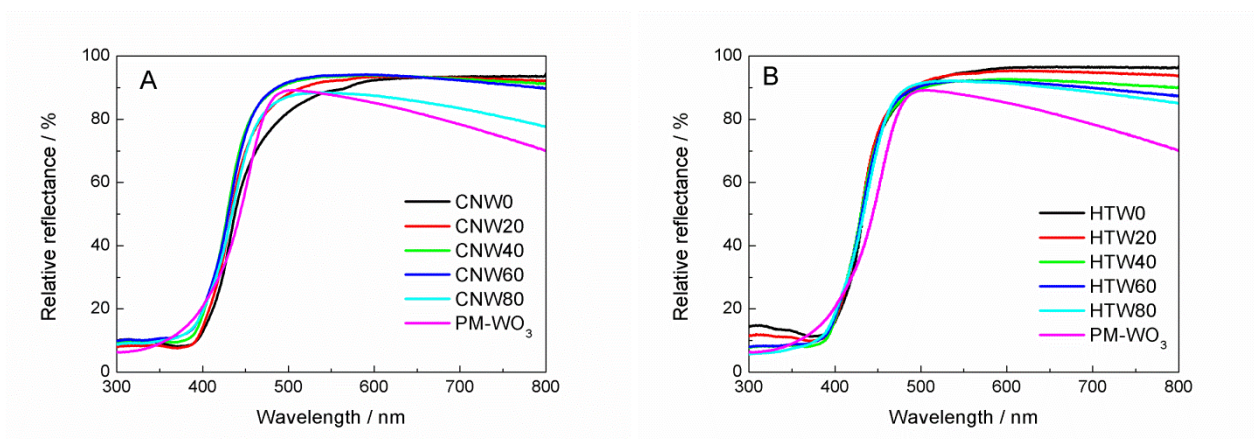


Fig. 7 UV-vis DR spectra of (A) CNW x , (B) HTW x and PM- WO_3 samples.

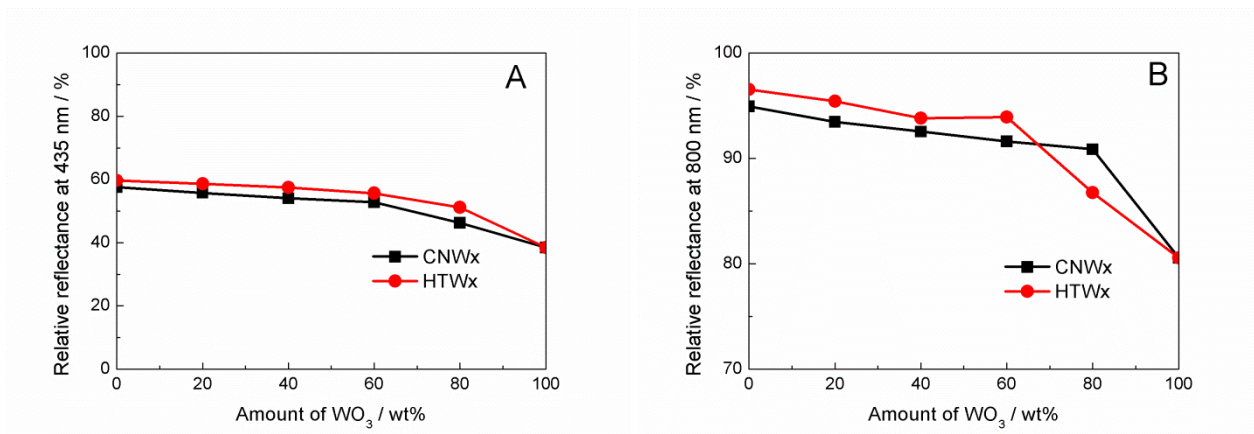


Fig. 8 Relative reflectance of CNW x and HTW x samples at the wavelength of (A) 435 nm and (B) 800nm as a function of WO_3 contents.

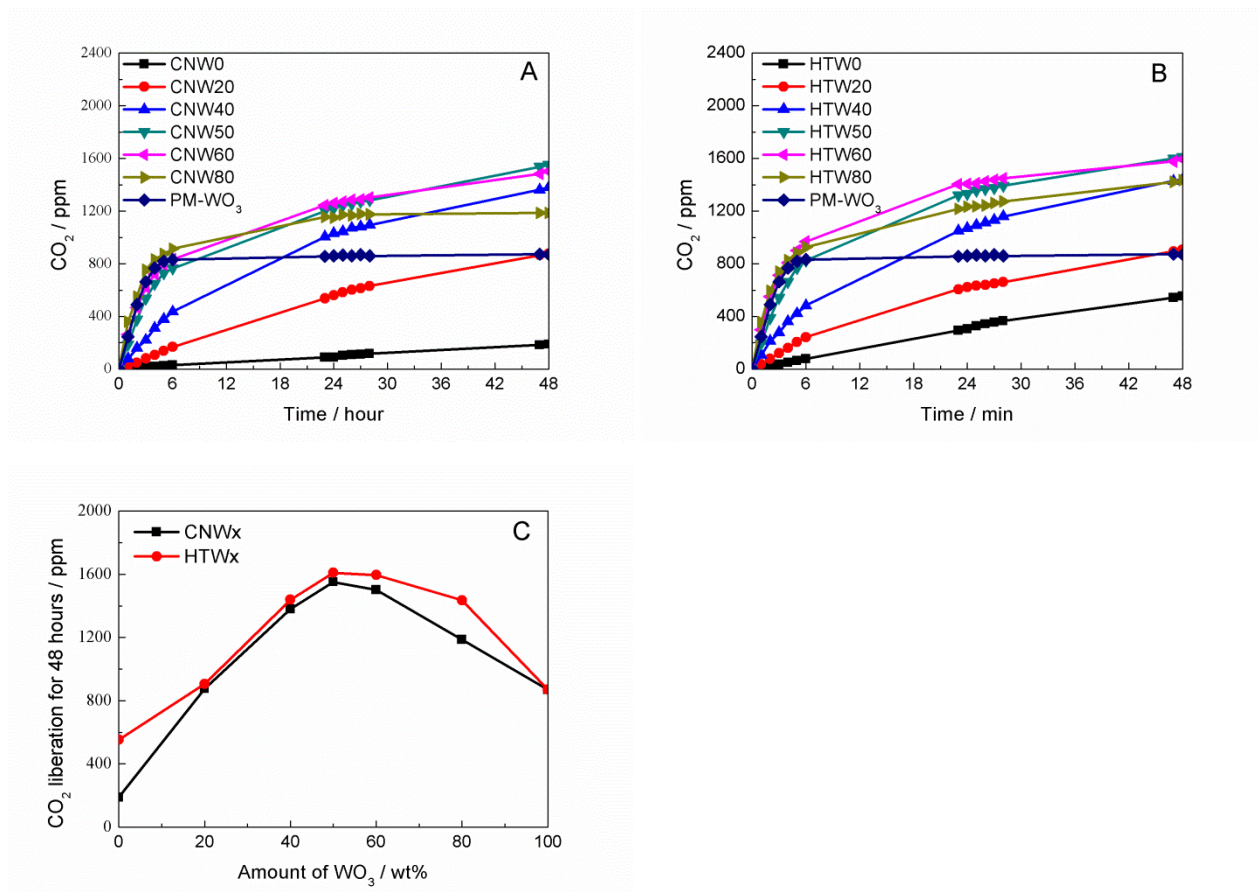


Fig. 9 Time courses of CO_2 liberation from acetaldehyde decomposition over (A) CNW_x and (B) HTW_x samples. (C) CO_2 liberation over CNW_x and HTW_x samples for 48 hours of photoirradiation as a function of WO_3 contents.

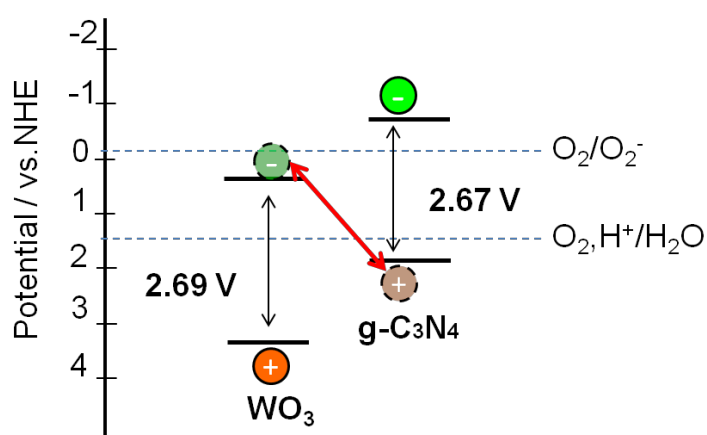


Fig. 10 Schematic band structure of $\text{g-C}_3\text{N}_4$ and WO_3 . The literature values for the band structure of $\text{g-C}_3\text{N}_4$ [32] and WO_3 [33] was used.